

Electronic Structure of Hemin in Solution Studied by Resonant X-ray Emission Spectroscopy and Electronic Structure Calculations

Kaan Atak,^{†,‡} Ronny Golnak,^{†,§} Jie Xiao,[†] Edlira Suljoti,[†] Mika Pflüger,^{†,‡} Tim Brandenburg,^{†,‡} Bernd Winter,[†] and Emad F. Aziz^{*,†,‡}

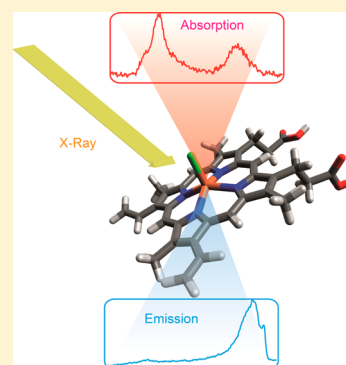
[†]Joint Laboratory for Ultrafast Dynamics in Solutions and at Interfaces (JULiq), Helmholtz-Zentrum Berlin für Materialien und Energie, Albert-Einstein-Strasse 15, 12489 Berlin, Germany

[‡]Fachbereich Physik, Freie Universität Berlin, Arnimallee 14, D-14195 Berlin, Germany

[§]Fachbereich Chemie, Freie Universität Berlin, Takustrasse 3, D-14195 Berlin, Germany

S Supporting Information

ABSTRACT: Resonant inelastic X-ray scattering spectra at the iron L-edge from hemin in dimethyl sulfoxide liquid solution are reported. Our experiments, which are interpreted with the help of electronic structure calculations, support earlier assignments of hemin–solvent interactions, including the iron spin state and the role of the chloride ligand obtained from a total fluorescence yield study. The analysis of the explicit radiative relaxation channels of 2p core-level excited iron, explored in the present work, allows for a rather quantitative assignment of the orbitals involved in the excitation–deexcitation process of the core-excited hemin in solution. We specifically distinguish between contributions of partially and fully occupied valence orbitals to the broad X-ray emission band. In addition, our calculations reveal a detailed picture of the character of these orbitals.



INTRODUCTION

Numerous proteins contain metalloporphyrins (MP) as functional groups, with transition metals (TM) in the porphyrin-ring center, allowing for a wide range of biological functions. The latter include oxygen storage and transport (hemoglobin (Hb), myoglobin (Mb)), electron transport (cytochrome oxidase), and energy conversion (chlorophyll), demonstrating photosensitive and catalytic properties.^{1–3} Porphyrin studies also extend to applications in the activation of human immunodeficiency virus.⁴ Due to the diversity of their functions, MPs remain subject of current spectroscopic investigations, porphyrin research continues to be an active field, and there is a focus on the configurational details, bonding, and spin states of the metal center.^{2,5} A startling feature of biological iron (such as in ferri-Hb or ferri-Mb) is its flexibility and adaptability of electronic properties which is less common in inorganic iron complexes. This unique feature originates from the small energy differences between different spin-state configurations.^{2,6,7} There is a strong correlation between molecular geometric structure and spin state, and the N–Fe–N bond angle is found to be dependent on the spin multiplicity of these porphyrin complexes.⁷ Depending on the chemical environment, different spin states can coexist, and additionally the spin state may change (spin crossover)⁸ as a function of ligand coordination.⁹ Understanding these mechanisms is extremely important for unraveling the transport properties of these biomolecules.¹⁰

For a description of the local electronic structure governing these properties, the orbital mixing between the transition metal ion and the surrounding porphyrin ring has to be investigated. From the experimental side, soft-X-ray spectroscopy is ideally suited for this purpose, providing an unprecedented sensitivity to local electronic structure, and is applicable for *in situ* investigations.^{11,12} For hemin in ethanol total fluorescence yield (TFY) X-ray absorption measurements at the iron L-edge¹⁰ (corresponding to electron promotion from Fe 2p to 3d level) revealed that the complex is in a high-spin state with iron being five-coordinated by nitrogens (equatorial) and chlorine (coaxial). In the present work, we explore the explicit radiative relaxation channels of core (2p) excited hemin in dimethyl sulfoxide (DMSO) solution. The respective resonant X-ray emission (or often referred to as resonant inelastic X-ray scattering, RIXS¹³) spectra, when integrated as a function of excitation photon energy yield approximately the aforementioned X-ray absorption (XA) spectra. Hence, the RIXS spectra, which contain additional information on the electronic structure of the core-excited solute, are one of the keys for a proper interpretation of XA spectra, solely based on experiment. The other complementary method would be based on the detection of the respective electron-out channel, but such resonant photoelectron studies

Received: May 25, 2014

Revised: July 3, 2014

Published: July 28, 2014

from low-concentration hemin solutions are yet elusive. In addition to explicitly studying the photon-out channels, we also performed post-Hartree–Fock restricted open-shell configuration interaction singles calculations (ROCIS) combined with density functional theory (DFT/ROCIS method),¹⁴ on the *ab initio* level. As we will show, our computational results confirm several key electronic-structure details of the hemin–solvent interactions already identified in a previous TFY-XA study.¹⁰

A major experimental challenge in performing RIXS measurements from hemin in solution is to obtain a reasonably large signal-to-noise ratio given the low solubility of hemin in many solutions. To this end, dimethyl sulfoxide solvent is a compromise, as we can obtain 50 mM concentrations which is more than 15 times larger than in our total-yield study of ref 10. Yet, this larger concentration is insufficient to compensate for the several experimental factors associated with using a spectrometer, leading to a reduction of the detected photon signal as compared to a TFY-XA measurement. In the latter case a sensitive photodiode can be positioned at a very short distance from the sample which strongly increases the number of detected photons. In fact, the obtained partial fluorescence yield (PFY) XA spectrum in the present work, which requires the measurement of many RIXS spectra (over many hours), is not as well-resolved as the TFY-XA spectrum of ref 10.

METHODS

Experiment. Both iron(III) protoporphyrin IX chloride (hemin, FePPIX) from bovine (purity > 90%) and the dimethyl sulfoxide solvent (purity > 99%; (CH₃)₂SO or DMSO) were obtained from Sigma-Aldrich. RIXS measurements at the Fe L-edge were performed from a solution of 50 mM FePPIX–chloride dissolved in DMSO. We used the LiXEdrom end-station equipped with a liquid flow cell^{10,15} at the U41-PGM undulator beamline of BESSY II, in Berlin. The flow cell incorporates a 100 nm thick Si₃N₄ membrane separating the solution from the vacuum. A detailed description of the setup is given in ref 16. Photons were detected using a Rowland-circle geometry spectrometer with a grating of 7.5 m radius and 1200 lines/mm, covering the soft-X-ray energy range of 400–1000 eV. The detector, which is operated at a pressure of approximately 10^{−8} mbar, consists of an MCP/phosphorus screen-stack and a CCD camera. The pressure in the experimental chamber is generally in the mid 10^{−6} mbar range. The energy resolution for the present experiment was set to approximately 0.5 eV for a photon energy of 700 eV.

Computation. All calculations were carried out with the ORCA program package.¹⁷ Molecular geometry optimizations were performed using the B3LYP^{18,19} DFT method together with the def2-TZVP(-f) basis set.²⁰ Transition energies and moments for L-edges were calculated with DFT/ROCIS using the same basis set. For DFT/ROCIS calculations, the B3LYP functional together with the parameters $c_1 = 0.18$, $c_2 = 0.20$, and $c_3 = 0.40$ was applied.¹⁴ These three universal parameters are to be distinguished from the empirical parameters in semi-empirical molecular-orbital theories. During the optimization calculations, the resolution of identity^{21–25} approximation was used by employing the def2-TZV/J basis set.²⁶ Numerical integrations during the DFT calculations were performed on a dense grid (ORCA grid4). L-edge absorption spectra were obtained from the calculated transition moments by applying a Gaussian-type broadening of 1 eV. The geometry calculations implied no symmetry. However, for simplicity, below we will analyze results in terms of square-planar and octahedral point

symmetry groups. Vibronic interference effects were not taken into account in the calculations.

RESULTS AND DISCUSSION

It is convenient to first consider the PFY-XA spectrum of iron at the L_{2,3}-edge, measured here, with the grating set to the first-order diffraction. The result is shown in Figure 1, top tier. For

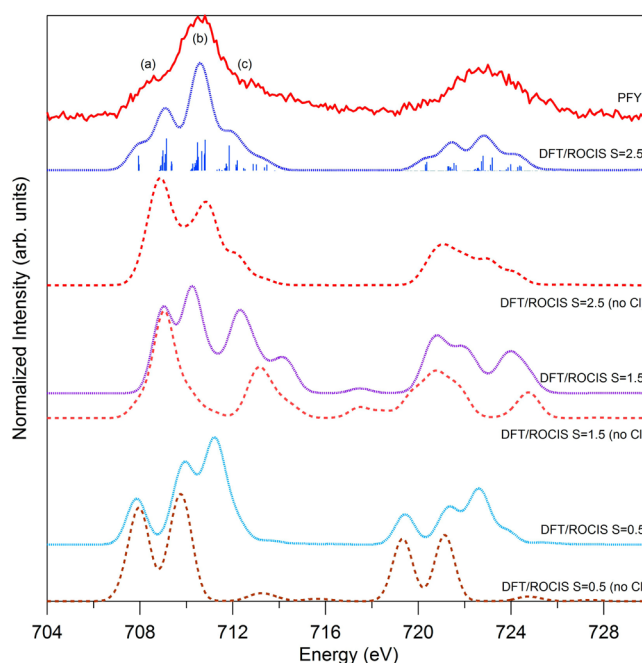


Figure 1. Experimental iron L-edge PFY spectrum (top red tier) of 50 mM FePPIX chloride solution in DMSO, compared to DFT/ROCIS XA spectrum calculations for different spin multiplicities, with chloride present and absent, respectively. The blue sticks represent the intensities of individual transitions. In the top tier, (a), (b), and (c) refer to the main absorption features discussed here.

the reasons given in the Introduction the signal-to-noise ratio of this spectrum is considerably less than the TFY-XA spectrum from hemin in ethanol reported in ref 10. This has no effect on the current work though where one goal is to determine the electronic structure of hemin in solution, from *ab initio* theory. Individual RIXS spectra, from which the experimental XA spectrum of Figure 1 is obtained through integration of the RIXS signal intensities, will be addressed later.

We next explore by theoretical simulation the effect of the existence of a nearby Cl[−] anion on the iron spin state and how this reflects in the spectra. Our approach is simple, treating spin state as a parameter, and we do not study the explicit molecular interactions between solute and solvent. Although it is already suggested in ref 10 that Cl[−] does not dissociate and that the high-spin state 2.5 is assumed (the ground-state electronic configuration of Fe³⁺ is 3d⁵), it is yet instructive to explore the effect of a hypothetical spin state on the XA spectrum. The theoretical XA spectra obtained from DFT/ROCIS calculations are shown underneath the experimental spectrum in Figure 1. Results for spin states $S = 2.5$, 1.5 , and 0.5 , calculated with the Cl[−] present and absent, respectively, are presented in the several tiers of the figure. Spectra are normalized to the highest intensity feature at the L₃-edge. Our calculations show that the high-spin case ($S = 2.5$), with chloride bound to the molecular ring, matches best with the experimental spectrum, in

agreement with ref 10. Interestingly, our results are inconsistent with conclusions based on UV–visible spectrophotometry studies which suggest that in DMSO solution the chloride is dissociated from FePIX.^{27,28}

We show in Figure 2 the computed structures within the same DFT calculations for a visualization of spin state on

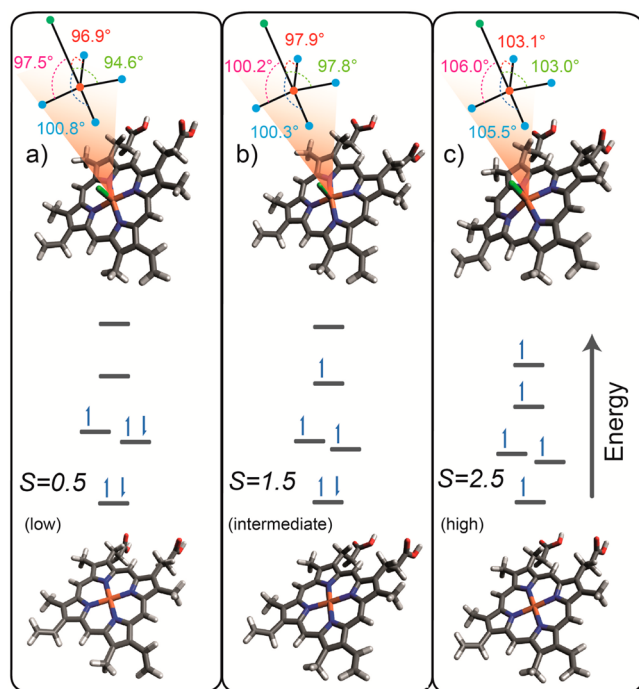


Figure 2. Simplified singly occupied iron d-orbital energy diagrams of the three different spin states and the molecular geometries of iron(III) protoporphyrin IX with and without a chloride at the top and the bottom, respectively.

geometry. It is seen that the effect of spin state on the molecular structure is more pronounced when chloride is included. In the higher spin-state structures the iron tends to pull away from the molecular ring plane; this is reflected in the increasing N–Fe–Cl bond angles in Figure 2 (and Table SI-1 of the Supporting Information, SI). The smaller effect of spins on structure in the absence of Cl[−] is best visualized through the numerical values of the Fe–N bond distances, presented in Table SI-2 of the SI.

So far we have simulated the XA spectrum from hemin in solution without an assignment of the peaks in the experimental PFY-XA spectrum of Figure 1 (top tier) to actual electronic transitions. For this we first calculate the transition energies in the absence of spin–orbit coupling (SOC), and then include SOC as a perturbation. Results for the SOC-excluded case are presented in SI Figure SI-1; states are well-defined and can be readily assigned to the experimental peaks. In contrast, inclusion of SOC, which is the more accurate description as we have seen previously, leads to an absorption spectrum characterized by thousands (>5000) of ionic multiplet states,²⁹ indicated by sticks in the second top tier of Figure 1. A specific orbital-character assignment of this large manifold of spin-mixed states is elusive. Our analysis shows though (see SI Figure SI-1) that the prominent transitions, represented by the bars, appear at very similar energies for both SOC included and excluded; in the latter case these states are however more spread, and each individual state contributes less to the total

spectrum. For our further electronic structure analysis it is thus sufficient to just consider the well-assigned orbitals of the SOC-excluded calculations. We can then employ a simpler one-electron picture description for interpreting the MO character and bonding structure. The actual computed spectrum results when representing each energy value by a Gaussian of 1 eV width; furthermore, calculated energies were shifted *ad hoc* by +17.5 eV in order to match with experiment. Such an energy shift is due to the intrinsic shortcomings of the density functionals used here.¹⁴ In our calculations we also find a similar ~1 eV underestimation of the energy difference between the L₂- and L₃-edges as reported by Roemelt et al.,¹⁴ who introduced the DFT/ROCIS method. This effect has no relevance for the interpretation of the experimental spectrum.

The experimental L₃-edge PFY-XA spectrum of Figure 1 exhibits three main features, a maximum peak at 710.5 eV (label b), a shoulder at 708.3 eV (label a) on the low-energy side, and another shoulder near 712.8 eV (label c) at the high-energy side. These are the same features reported in a previous total-yield study,¹⁰ although peaks are less resolved in the present partial-yield study; see the preceding given reasons. The resolution in the L₂-edge region is not high enough to clearly distinguish the discrete features, appearing here only as repeating faint structures at 720.8, 722.8, and 725.0 eV. To assign the features of the L₃-edge XA spectrum to electronic transitions, we return to the computation scheme described in the previous paragraph, and for the reasons mentioned above we will consider the *S* = 2.5 case with SOC excluded. Calculated energies are presented in SI Figure SI-1. Four energy positions can be identified where prominent transitions occur, 708.0, 709.1, 710.4, and 710.9 eV. The first two constitute the feature a, and the two latter transitions form the feature b of the experimental XA spectrum. From Table 1 where the computed molecular-orbital (MO) characters are presented in detail it is seen that MO 167 is responsible for the first transition which itself is the first singly occupied molecular orbital (SOMO). The second transition is comprised of MOs 168 and 169, implying a very small energetic difference between

Table 1. Character of MOs of the Single-Point DFT Calculations Illustrating the Mixing of the Iron d-Orbitals in FePIX Chloride As Inferred from Restricted Open-Shell Single-Point DFT Calculation, Combined with Löwdin Population Analysis

orbital no.	energy (eV)	main iron d-orbital contribution (and proposed character)	main atomic contributions from Fe and its nearest neighbors
171	−8.38	73.4% d _{x²−y²} (σ*)	74.3% Fe, 19.0% N
170	−8.74	69.2% d _{z²} (σ*)	72.0% Fe, 12.8% Cl, 8.2% N
169	−10.37	83.1% d _{xz} (π*)	86.3% Fe, 6.7% Cl, 4.1% N
168	−10.39	83.9% d _{yz} (π*)	86.4% Fe, 6.7% Cl, 4.0% N
167	−11.70	96.6% d _{xy} (π*)	97.6% Fe, 1.2% N
165	−5.84	2.7% d _{z²} (σ)	8.8% N, 3.9% Fe, 1.3% Cl
161	−6.98	3.2% d _{z²} (σ)	23.5% N, 5.6% Cl, 5.1% Fe
157	−7.94	6.4% d _{xz} , 3.1% d _{yz} (π)	61.3% Cl, 11.1% Fe, 3.1% N
155	−7.98	2.3% d _{xz} , 4.0% d _{yz} (π)	36.5% Cl, 7.3% Fe, 3.0% N
152	−9.01	0.9% d _{xz} , 2.4% d _{yz} (π)	23.4% N, 6.2% Fe
151	−9.04	1.4% d _{xz} , 1.1% d _{yz} (π)	16.7% N, 4.5% Fe
147	−9.25	7.5% d _{x²−y²} (σ)	10.0% N, 7.8% Fe
146	−9.41	20.1% d _{z²} (σ)	72.8% Cl, 24.8% Fe

these orbitals in the core-hole-excited state. The last two transitions are due to MOs 170 and 171, respectively. All five MOs (167–171) are singly occupied iron d-orbitals constituting the π^* and σ^* antibonding MOs which will be discussed later. The computational results do not indicate any significant contributions from transitions involving unoccupied MOs; these are the ones with numbers ≥ 172 . Unlike peaks (a) and (b), peak (c) is only reproduced (see SI Figure SI-1) when SOC effects are included which allows for mixing of orbital spins, causing the aforementioned multiplet structure.

The five SOMOs, identified in the previous paragraph, which give the XA spectrum its characteristic shape deserve more attention due to the information they provide on bonding. Here we refer back to Table 1 where the atomic contributions from iron and from nearest neighbors are presented; we also explicitly quantify the d-orbital contributions from iron using Löwdin population analysis. The identified five orbitals are seen to be primarily iron d-orbitals with antibonding character; see also Figure 3 which presents the MO energies and spatial

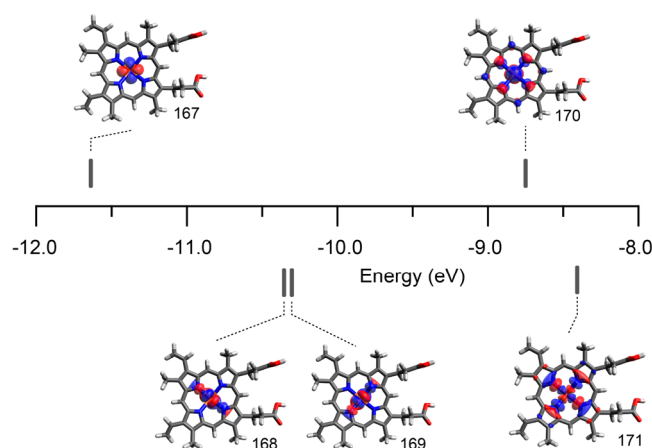


Figure 3. Iron 3d-orbitals of FePPIX chloride with $S = 2.5$ according to the B3LYP/def2-TZVP(-f)/def2-TZV/J restricted open-shell single-point DFT calculation.

distributions for these orbitals. According to the population analysis, higher-energy unoccupied orbitals have significantly more ligand character. In the absorption process, the involvement of these orbitals would imply metal-to-ligand charge-transfer transitions; however this is not the case. The antibonding MOs 167–171 hint at σ and π bonds in the form of bonding MOs (Table 1). However, similar to the findings by Hocking et al.³⁰ for $[\text{Fe}(\text{tpp})(\text{ImH})_2]^+$ involving ferric iron, back-bonding cannot be unequivocally identified. This supports the conclusion that hemin solvated in DMSO is in the high-spin state since back-bonding would increase the bond strength between the TM ion and the ligands, likely causing larger orbital splitting and hence leading to a low-spin state. We also note that the actual symmetry of the ligand structure is inferred here from experiment and computation, combined. Peak (a) in the experimental spectrum implies degeneracy of d_{xz} -based and d_{yz} -based orbitals (observed in both the DFT/ROCIS and the single-point calculations; refer to Table 1) which is indicative of C_{4v} symmetry ligand structure. An octahedral ligand field, for instance, causing low-spin configuration would lead to a considerably different shape of the XA spectrum, inconsistent with experiment.

We now turn to the RIXS spectra presented in Figure 4 and extract the additional information on electronic structure these

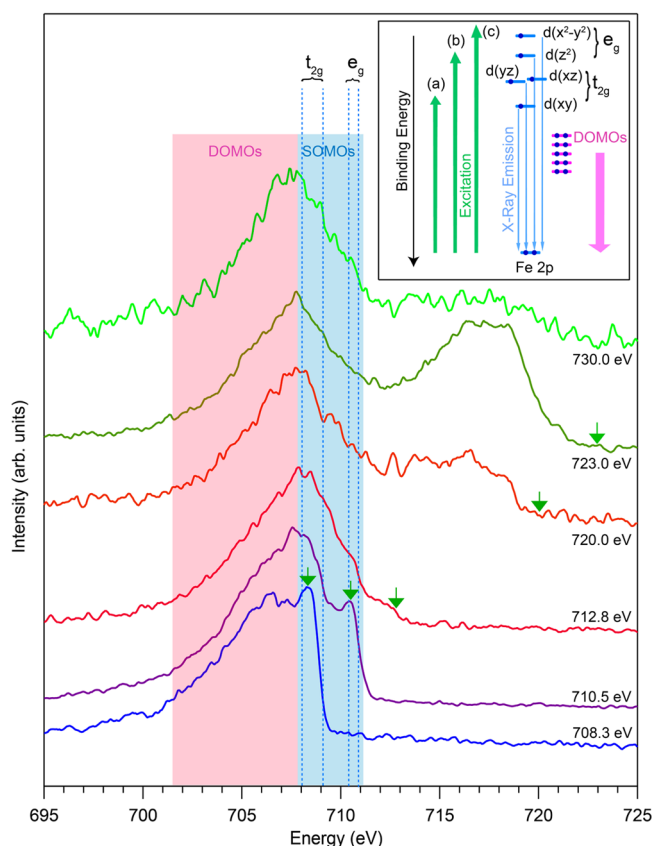


Figure 4. Iron L-edge RIXS spectra from 50 mM FePPIX–chloride solution. The inset is a simplified schematic representation of observed X-ray excitation and de-excitation transitions.

spectra provide; here we focus on the L_3 -edge. These spectra were measured separately, for an extended collection time (~ 1 h per RIXS spectrum) at the photon energies corresponding to aforementioned preabsorption (a), main absorption (b), and postabsorption (c) energies, at 708.3, 710.5, and 712.8 eV, respectively. Note that the full-range PFY-XA spectrum in Figure 1 has been obtained for a much shorter acquisition time per RIXS spectrum, but many more spectra were recorded (in steps of 0.1 eV excitation photon energy) over the same photon-emission range as displayed in Figure 4. Simulation of L-edge RIXS spectra has not yet been incorporated into the ORCA suite (refer to ORCA manual),³¹ and we attempt an interpretation of the experimental RIXS spectra using a simplified orbital picture combining the results of single-point DFT and DFT/ROCIS calculations. Qualitative inspection of the L_3 -edge RIXS spectra reveals an almost identical emission spectrum in the approximately 700–712 eV photon energy range. This is clear experimental evidence that 3d–3d and 3d–2p electron correlation is rather weak, which is a surprising result for this 3d metal complex. Note that the higher energy part of the emission spectrum (shown by blue shading) is absent for the pre- and main-edge excitation, in which case this energy region coincides with the inelastic emission peak (shown by the small arrows in the spectra). The large intensity of the elastic peak for the lower excitation energies is in line with our previous findings for simpler iron complexes.³² Intensity in the 715–720 eV region, occurring in the three

uppermost RIXS spectra, arises from L_2 -edge excitation but is not further considered here. For a more quantitative interpretation of the RIXS spectra we consider the energy-level diagram shown as an inset in Figure 4. Here we depict the three main excitations, at energies (a), (b) and (c) of the XA spectrum (of Figure 1), along with the calculated Fe 3d energies (from DFT/ROCIS and ignoring the SOC originated L_2 – L_3 separation), and we also include the doubly occupied molecular orbitals (DOMO). These latter orbitals have both iron and ligand contributions (compare Table 1 and SI Figure SI-2) and are thus interpreted as ligand-to-metal charge-transfer transitions (LMCT). Fe 2p to valence excitations are represented by the green arrows, and the radiative decays are illustrated by blue (transitions from SOMOs to Fe 2p) and red (transitions from DOMOs) arrows, respectively. As depicted in the diagram, post-edge excitations, at 712.8 eV (and all higher excitation energies), lead to the population of all SOMOs, d_{xy} through $d_{x^2-y^2}$, and emission from each one can be expected. These transitions correspond to the high-energy side (blue shaded) of the experimental RIXS spectra, and here we notice a very good quantitative agreement between experiment and theory. It is obvious from the calculated energies that the low-energy side (red shaded) of the emission band of Figure 4 must be due to the valence DOMO \rightarrow Fe 2p transitions, and we can in fact determine the valence DOMO energies from the experimental emission energies. This would put the emitting DOMOs in a 6 eV energy band lying below the SOMO energies. The fact that experimental energies are well-matching with the relative energies determined here (see Figure 3, SI Figure SI-2, and Table 1) is another indication of the previously mentioned small 3d correlation, or alternatively the extra charge being smeared out due to the high density of states.

CONCLUSION

We have reported the first L-edge RIXS spectra from hemin in liquid solution. Aided by *ab initio* calculations the emission spectra can be almost quantitatively interpreted in terms of the orbitals involved in the excitation–de-excitation processes. From the RIXS spectra we also construct the so-called partial fluorescence yield X-ray absorption spectrum which can be interpreted more accurately than previous spectra based on total-yield measurements. Overall, our experimental and computational findings are in qualitative accordance with previous results, essentially supporting a hemin–Cl structure in high-spin configuration.

ASSOCIATED CONTENT

Supporting Information

Text describing computation details and accompanying references, tables listing coordination of FePPIXCl and FePPIX with different spin configurations, and figures showing experimental iron L-edge PFY spectra and inner valence molecular orbitals of FePPIXCl. This material is available free of charge via the Internet at <http://pubs.acs.org>.

AUTHOR INFORMATION

Corresponding Author

*E-mail: emad.aziz@helmholtz-berlin.de.

Notes

The authors declare no competing financial interest.

ACKNOWLEDGMENTS

This work was supported by the European Research Council Starting Grant No. 279344 and Helmholtz-Gemeinschaft via the young investigator fund VH-NG-635. K. A. acknowledges the financial support of the Einstein Foundation Berlin for the postdoctoral scholarship.

REFERENCES

- (1) Milgrom, L. R. *The Colours of Life: An Introduction to the Chemistry of Porphyrins and Related Compounds*; Oxford University Press: New York, NY, USA, 1997.
- (2) Charkin, O. P.; Klimenko, N. M.; Charkin, D. O.; Chang, H.-C.; Lin, S.-H. Theoretical DFT Study of Fragmentation and Association of Heme and Hemin. *J. Phys. Chem. A* **2007**, *111*, 9207–9217.
- (3) Bergmann, N.; Bonhommeau, S.; Lange, K. M.; Greil, S. M.; Eisebitt, S.; de Groot, F.; Chergui, M.; Aziz, E. F. On the Enzymatic Activity of Catalase: An Iron L-Edge X-Ray Absorption Study of the Active Centre. *Phys. Chem. Chem. Phys.* **2010**, *12*, 4827–4832.
- (4) Vzorov, A. N.; Dixon, D. W.; Trommel, J. S.; Marzilli, L. G.; Compans, R. W. Inactivation of Human Immunodeficiency Virus Type 1 by Porphyrins. *Antimicrob. Agents Chemother.* **2002**, *46*, 3917–3925.
- (5) Koenig, D. F. The Structure of A-Chlorohemin. *Acta Crystallogr.* **1965**, *18*, 663–673.
- (6) Kotani, M. Electronic Structure of Iron in Porphyrin Complexes. *Ann. N. Y. Acad. Sci.* **1969**, *158*, 20–49.
- (7) Suchkova, S. A.; Soldatov, A.; Dziedzic-Kocurek, K.; Stillman, M. J. The Role of Spin State on the Local Atomic and Electronic Structures of Some Metalloporphyrin Complexes. *J. Phys.: Conf. Ser.* **2009**, *190*, 012211.
- (8) Gütllich, P.; Gaspar, A. B.; Garcia, Y. Spin State Switching in Iron Coordination Compounds. *Beilstein J. Org. Chem.* **2013**, *9*, 342–391.
- (9) Harada, Y.; Taguchi, M.; Miyajima, Y.; Tokushima, T.; Horikawa, Y.; Chainani, A.; Shiro, Y.; Senba, Y.; Ohashi, H.; Fukuyama, H.; et al. Ligand Energy Controls the Heme-Fe Valence in Aqueous Myoglobins. *J. Phys. Soc. Jpn.* **2009**, *78*, No. 044802.
- (10) Aziz, E. F.; Ottosson, N.; Bonhommeau, S.; Bergmann, N.; Eberhardt, W.; Chergui, M. Probing the Electronic Structure of the Hemoglobin Active Center in Physiological Solutions. *Phys. Rev. Lett.* **2009**, *102*, No. 068103.
- (11) Aziz, E. F.; Ottosson, N.; Faubel, M.; Hertel, I. V.; Winter, B. Interaction between Liquid Water and Hydroxide Revealed by Core-Hole de-Excitation. *Nature* **2008**, *455*, 89–91.
- (12) Mitzner, R.; Rehanek, J.; Kern, J.; Gul, S.; Hattne, J.; Taguchi, T.; Alonso-Mori, R.; Tran, R.; Weniger, C.; Schröder, H.; et al. L-Edge X-ray Absorption Spectroscopy of Dilute Systems Relevant to Metalloproteins Using an X-ray Free-Electron Laser. *J. Phys. Chem. Lett.* **2013**, *4*, 3641–3647.
- (13) de Groot, F.; Kotani, A. *Core Level Spectroscopy of Solids*; CRC Press: Boca Raton, FL, USA, 2008.
- (14) Roemelt, M.; Maganas, D.; DeBeer, S.; Neese, F. A Combined DFT and Restricted Open-Shell Configuration Interaction Method Including Spin-Orbit Coupling: Application to Transition Metal L-Edge X-Ray Absorption Spectroscopy. *J. Chem. Phys.* **2013**, *138*, No. 204101.
- (15) Tokushima, T.; Horikawa, Y.; Harada, Y.; Takahashi, O.; Hiraya, A.; Shin, S. Selective Observation of the Two Oxygen Atoms at Different Sites in the Carboxyl Group (–COOH) of Liquid Acetic Acid. *Phys. Chem. Chem. Phys.* **2009**, *11*, 1679.
- (16) Lange, K. M.; Könncke, R.; Ghadimi, S.; Golnak, R.; Soldatov, M. A.; Hodeck, K. F.; Soldatov, A.; Aziz, E. F. High Resolution X-Ray Emission Spectroscopy of Water and Aqueous Ions Using the Micro-Jet Technique. *Chem. Phys.* **2010**, *377*, 1–5.
- (17) Neese, F. The ORCA Program System. *Wiley Interdiscip. Rev.: Comput. Mol. Sci.* **2012**, *2*, 73–78.
- (18) Becke, A. D. Density-Functional Exchange-Energy Approximation with Correct Asymptotic Behavior. *Phys. Rev. A* **1988**, *38*, 3098–3100.

- (19) Becke, A. D. Density-Functional Thermochemistry. III. The Role of Exact Exchange. *J. Chem. Phys.* **1993**, *98*, 5648–5652.
- (20) Weigend, F.; Ahlrichs, R. Balanced Basis Sets of Split Valence, Triple Zeta Valence and Quadruple Zeta Valence Quality for H to Rn: Design and Assessment of Accuracy. *Phys. Chem. Chem. Phys.* **2005**, *7*, 3297–3305.
- (21) Baerends, E. J.; Ellis, D. E.; Ros, P. Self-Consistent Molecular Hartree—Fock—Slater Calculations I. The Computational Procedure. *Chem. Phys.* **1973**, *2*, 41–51.
- (22) Dunlap, B. I.; Connolly, J. W. D.; Sabin, J. R. On Some Approximations in Applications of $X\alpha$ Theory. *J. Chem. Phys.* **2008**, *71*, 3396–3402.
- (23) Vahtras, O.; Almlöf, J.; Feyereisen, M. W. Integral Approximations for LCAO-SCF Calculations. *Chem. Phys. Lett.* **1993**, *213*, 514–518.
- (24) Eichkorn, K.; Treutler, O.; Öhm, H.; Häser, M.; Ahlrichs, R. Auxiliary Basis Sets to Approximate Coulomb Potentials. *Chem. Phys. Lett.* **1995**, *240*, 283–290.
- (25) Eichkorn, K.; Weigend, F.; Treutler, O.; Ahlrichs, R. Auxiliary Basis Sets for Main Row Atoms and Transition Metals and Their Use to Approximate Coulomb Potentials. *Theor. Chem. Acc.* **1997**, *97*, 119–124.
- (26) Weigend, F. Accurate Coulomb-Fitting Basis Sets for H to Rn. *Phys. Chem. Chem. Phys.* **2006**, *8*, 1057–1065.
- (27) Collier, G. S.; Pratt, J. M.; De Wet, C. R.; Tshabalala, C. F. Studies on haemin in dimethyl sulfoxide/water mixtures. *Biochem. J.* **1979**, *179*, 281–289.
- (28) Adams, P. A.; Baldwin, D. A.; Hepner, C. E.; Pratt, J. M. Coordination of Imidazole by Hemin in Organic and Aqueous Organic Solvents. *Bioinorg. Chem.* **1978**, *9*, 479–494.
- (29) Jensen, F. *Introduction to Computational Chemistry*; John Wiley & Sons: Chichester, England; Hoboken, NJ, USA, 2007.
- (30) Hocking, R. K.; Wasinger, E. C.; Yan, Y.-L.; deGroot, F. M. F.; Walker, F. A.; Hodgson, K. O.; Hedman, B.; Solomon, E. I. Fe L-Edge X-ray Absorption Spectroscopy of Low-Spin Heme Relative to Non-Heme Fe Complexes: Delocalization of Fe d-Electrons into the Porphyrin Ligand. *J. Am. Chem. Soc.* **2006**, *129*, 113–125.
- (31) Neese, F. The ORCA program system. *WIREs Comput. Mol. Sci.* **2012**, *2*, 73–78.
- (32) Atak, K.; Bokarev, S. I.; Gotz, M.; Golnak, R.; Lange, K. M.; Engel, N.; Dantz, M.; Suljoti, E.; Kühn, O.; Aziz, E. F. Nature of the Chemical Bond of Aqueous Fe^{2+} Probed by Soft X-ray Spectroscopies and ab Initio Calculations. *J. Phys. Chem. B* **2013**, *117*, 12613–12618.